Boosting CO2 reforming of methane via the metal-support interaction in mesostructured SBA-16-derived Ni nanoparticles

Chao Sun, Paulina Summa, Ye Wang, Katarzyna Świrk, Albert Miró I Rovira, Sandra Casale, Konrad Świerczek, Changwei Hu, Magnus Rønning, Patrick da Costa

Boosting CO_2 reforming of methane via the metal-support interaction in mesostructured SBA-16-derived Ni nanoparticles

Chao Sun [a,*], Paulina Summa [a,b], Ye Wang [a,f], Katarzyna Świrk [c], Albert Miró i Rovira [c], Sandra Casale [d], Konrad Świerczek [b], Changwei Hu [e,f], Magnus Rønning [c], Patrick Da Costa [a,*]

[a] Institut Jean Le Rond d'Alembert, Sorbonne Université, CNRS UMR 7190, 2 Place de la Gare de Ceinture, 78210 Saint-Cyr-l'Ecole, France.

[b] AGH University of Science and Technology, Faculty of Energy and Fuels, Al. A. Mickiewicza 30, 30-059, Krakow, Poland.

[c] Department of Chemical Engineering, Norwegian University of Science and Technology (NTNU), Sem Sælands vei 4, 7491 Trondheim, Norway.

[d] Laboratoire de Réactivité de Surface, Sorbonne Université, CNRS UMR 7197, 4 Place Jussieu, 75005 Paris, France.

[e] Key Laboratory of Green Chemistry and Technology, Ministry of Education, College of Chemistry, Sichuan University, 610064 Chengdu, China.

[f] College of Chemical Engineering, Sichuan University, 610065 Chengdu, China.

[*]Corresponding author:
Email address: chao.sun@dalembert.upmc.fr; patrick.da_costa@sorbonne-universite.fr ;

Abstract:

High surface area and porosity SBA-16 was synthesized and used as support for Ni nanoparticles using three methods including wet impregnation, citric acid-assisted impregnation, and ammonia evaporation. All the studied samples showed high activity in the CO_2 reforming of methane reaction, however, the best catalytic behavior was found for the catalyst derived from ammonia evaporation. Based on characterization techniques, it was assumed that the improvement in Ni/SBA-16-AE performance was due to the strong metal-support interaction resulting from the formation of Ni-phyllosilicate. Additionally, a high Ni dispersion was observed which may be related to the confinement of cage-like pores of the SBA-16 matrix. The ammonia evaporation technique can well contribute to the limited sintering of Ni nanoparticles and reduced amount of deposited carbon.

Keywords: SBA-16, Ni nanoparticles, Phyllosilicate, CO_2 reforming of methane, metal-support interaction, Ni dispersion.

1. Introduction

CO_2 emissions from anthropogenic sources such as combustion of fossil fuels and factory emissions have caused significant environmental issues and especially global warming [1]. In the past decades, the CO_2 capture, storage or utilization have been considered in order to reduce CO_2 emissions and convert CO_2 to useful resources [2–4]. CO_2 chemical conversion routes provide possibilities to convert CO_2 to fuels or value-added chemicals, showing potential to achieve a carbon neutral society [5–7]. CO_2 reforming of methane (CRM) ($CH_4 + CO_2 = 2CO + 2H_2$) can not only help to reduce the emissions of greenhouse gases (CO_2 and methane) but also produce syngas with appropriate H_2/CO ratio (1/1), which can be used to synthesize high-value fuels and chemicals by Fischer-Tropsch synthesis or other reactions [8–11]. In particular, supported nickel materials have been considered as appropriate catalysts for the reaction due to their high activity, selectivity, and low cost [9]. However, most of the Ni-based catalysts encounter the problem of low stability caused by the sintering of the active metal and by carbon deposition [12]. In the last years, many efforts have been devoted to develop catalysts with high activity and low carbon deposition [13–19]. Ni nanoparticles with small particle size was proved to alleviate the carbon deposition due to high saturation concentration of carbonaceous species on the small particles [20,21]. To obtain Ni catalysts with small Ni particle size, materials with high surface area and porosity such as mesoporous silica and alumina were developed [9,22–25]. Meanwhile, the strong metal-support interaction (MSI) can limit the sintering of Ni particles at high reaction temperature, which consequently improves the stability of Ni catalysts [26,27]. In the last years,

three-dimensional ordered mesoporous materials like SBA-16 have been used to prepare Ni catalysts for CO_2 reforming of methane due to their high surface area and porosity [9,28,29]. Such reported Ni/SBA-16 catalysts doped by cerium showed high activity and stability in the CRM reaction [9,29].

The objective of this study was to synthetize Ni-based SBA-16 with high surface area, high porosity, containing small Ni° particle size with strong MSI. Thus, three synthesis strategies were adopted. Citric acid and ammonia were used to obtain strong MSI on Ni catalysts in which the phyllosilicate structure from the ammonia evaporation method showed the strongest MSI [30,31]. Accordingly, for the first time Ni phyllosilicates SBA-16 and citric acid derived Ni/SBA-16 catalysts were used in dry (CO_2) reforming of methane. The catalysts were investigated for various synthesis strategies and tested for their reducibility, metal-support interaction, and catalytic performance.

2. Experimental

2.1 Materials Synthesis and Characterization

Ni/SBA-16 catalysts were prepared by using three synthesis strategies: i.e., wet impregnation (WI), citric acid-assisted wet impregnation (CA), and ammonia evaporation (AE). The as-prepared materials were labelled as Ni/SBA-16-WI, Ni/SBA-16-CA, and Ni/SBA-16-AE, respectively. The details of the catalysts synthesis are given in Supporting Information (SI).

N_2 adsorption measurement was conducted on a Belsorp Mini II apparatus (BEL Japan Inc.) with the detailed process described in our previous study [32]. The small-angle X-ray scattering (SAXS) was obtained from 0.5 to 5.0° with a 2θ step size of 0.01° on a Bruker D8 using Cu $K\alpha$ radiation (λ=1.5406Å). The wide-angle X-ray diffraction (XRD) was performed on a

diffractometer (PANalytical-Empyrean) equipped with a Cu $K\alpha$ radiation source (λ = 0.15406 nm, 40 kV, 40 mA). The signal was recorded at 10-90° with a 2θ step size of 0.02°. The H_2-TPR and CO_2-TPD experiments were conducted on an BELCAT-M apparatus (BEL Japan Inc.) equipped with a TCD with details given in our previous publication [33]. TGA was performed on the catalysts after activity tests on a Q5000 IR apparatus [34]. Transition Electronic Microscopy (TEM), HRTEM, and EDS experiments were performed on a JEM-2010 UHR (JEOL, Tokyo, Japan) apparatus for the reduced and spent catalysts [33].

2.2 CRM activity and stability catalytic tests

The CO_2 reforming of methane (CRM) activity and stability tests were conducted in a fixed-bed U-shaped reactor at 700-750°C under atmospheric pressure using a K-type thermocouple for monitoring the temperature. Before testing, 0.25 mL of sample was reduced at 800°C in a mixture of 5%H_2/Ar for 1 h. The reaction gas mixture was CO_2/CH_4/Ar=30/30/40 (100 mL/min) with gas hourly space velocity (GHSV) of 24,000 h^{-1}. The reaction was kept at each temperature for 1 h in order to reach steady-state, with outlet gases analyzed by a micro-GC (490 Varian Micro-GC). To study the stability of the catalysts, the reaction was kept at 700°C for 10 h. The conversion, reaction rate, and H_2/CO ratio were calculated by equations (4, 5, 6, 7.1 and 7.2) as shown in the Supporting Information (SI).

3. Results and discussion

3.1 Textural, structural, and morphology of materials

The textural properties of the materials obtained from N_2 isotherms and pore size distribution curves are displayed in **Fig.1**. The specific surface area (SSA), pore volume (V_p), and mean pore size (D_p) are also presented in **Table 1**. As reported in **Fig.1a**, all studied materials show a type-

IV isotherm according to IUPAC classification accompanied by a H_2 hysteresis loop at relative pressure (p/p_0) of 0.40-0.72, indicating the ink-bottle pores with structure of SBA-16 [9,35]. The Ni/SBA-16-AE catalyst showed a type-IV isotherm with a H_2 hysteresis loop at a wide relative pressure range of 0.5-0.95. Compared to Ni/SBA-16-WI and Ni/SBA-16-CA, the inflection point of Ni/SBA-16-AE shifted to higher p/p_0, indicating larger mesopores and broader pore size distribution [31,36]. This is in line with the results of BJH pore size distribution (**Fig.1b**). As shown in **Fig.1b**, SBA-16, Ni/SBA-16-WI and Ni/SBA-16-CA show primary mesopores at 3.1-3.6 nm. However, the Ni/SBA-16-AE catalyst also showed a broader pore size distribution at 2.5-15 nm with two primary mesopores with diameter of 4.0 and 10.7 nm.

As listed in **Table 1**, the as-synthesized SBA-16 presented a very high specific surface area (SSA) which is even higher than those reported in literature [9,35]. After the addition of nickel, the SSA and pore volume (V_p) of all Ni/SBA-16 catalysts decreased in contrast to the bare SBA-16 support. This can be assigned to the deposition of Ni species on the surface and pores of the support [9]. Among all the studied catalysts, the highest decrease in SSA was observed on Ni/SBA-16-AE. Previous studies [31,37] have shown that the dissolution or digestion of silica is unavoidable in the alkaline condition. In the current study, we used ammonia as precipitation reagent which provides very strong alkaline conditions and can explain the high decrease of SSA in the AE sample. Also, Ni/SBA-16-AE exhibited a broader average pore diameter distribution (D_p), which was caused by the collapse of small pores and the partial collapse of mesopores during the preparation process [31,38].

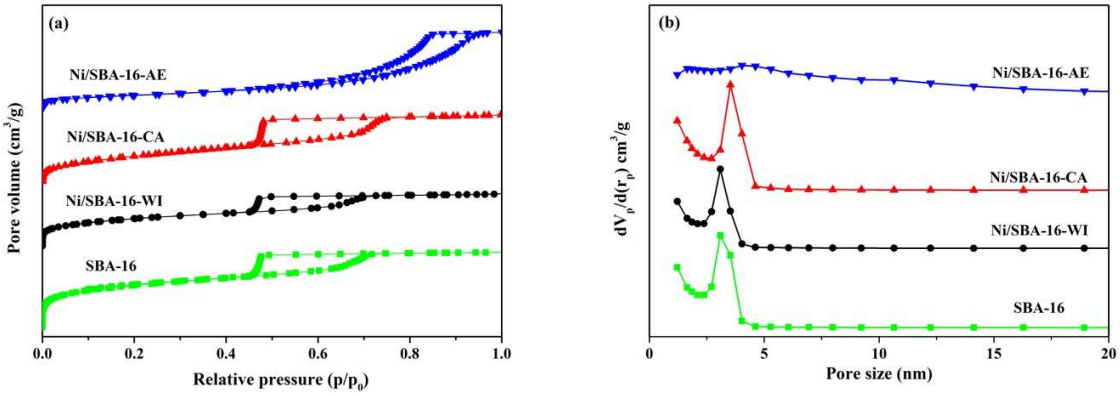

Figure. 1. N_2 adsorption-desorption isotherms (a) and pore size distribution curves (b) calculated by the BJH method for desorption branch of calcined samples.

Small-angle X-ray scattering was used to analyze the structural information of the SBA-16 material. The support showed a strong diffraction peak at 2θ=0.88° and two small peaks located at 2θ=1.42 and 1.57°, respectively (**Fig. S1**). These peaks can be assigned to the (110), (200), and (211) planes of SBA-16. This later result indicates the existence of ordered mesoporous SBA-16 with body-centered cubic symmetry (*Im3m*) [9,35].

Table 1 Physicochemical properties of the SBA-16 support and the Ni/SBA-16 catalysts (calcined and reduced).

Catalyst	SSA [a] (m^2/g)	V_p [b](cm^3/g)	D_p (nm) [b]	d_{NiO} (nm) [c]	d_{Ni} (nm) [c]	d_{Ni} (nm)	D_{Ni} (%)[d]
				calcined	reduced	from TEM	from TEM
SBA-16	1011	0.87	3.1	-	-	-	-
Ni/SBA-16-WI	675	0.63	3.1	8	5	9	10.0
Ni/SBA-16-CA	693	0.57	3.5	9	4	8	12.1
Ni/SBA-16-AE	301	0.69	4.0	-	3	6	16.4

[a] Calculated by BET method.
[b] Calculated by BJH method.
[c] Calculated from Scherrer equation [33].
[d] Calculated by equation 3 (Supporting Information).

The structural evolution of catalysts after calcination and reduction was investigated by XRD (**Fig.2**). One can note that on calcined materials the diffraction peaks at 2θ=37.0, 43.1, and 62.8° correspond to the presence of (111), (200), and (220) planes of the NiO phase, respectively [31,39,40] (**Fig.2a**). For Ni/SBA-16-AE, the diffraction peaks of NiO species are negligible, indicating a high dispersion of Ni species over the support. Only for Ni/SBA-16-AE, three new peaks located at 2θ=34.2, 36.4, and 60.8° are corresponding to the diffraction planes (200), (211), and (060) of Ni phyllosilicate are identified [31,41]. In **Fig.2b**, for the reduced materials, only the diffraction peaks corresponding to metallic Ni were detected. These peaks centered at 2θ=44.7, 51.9, and 76.5 correspond to the (111), (200) and (220) planes of metallic Ni, respectively [32–34].

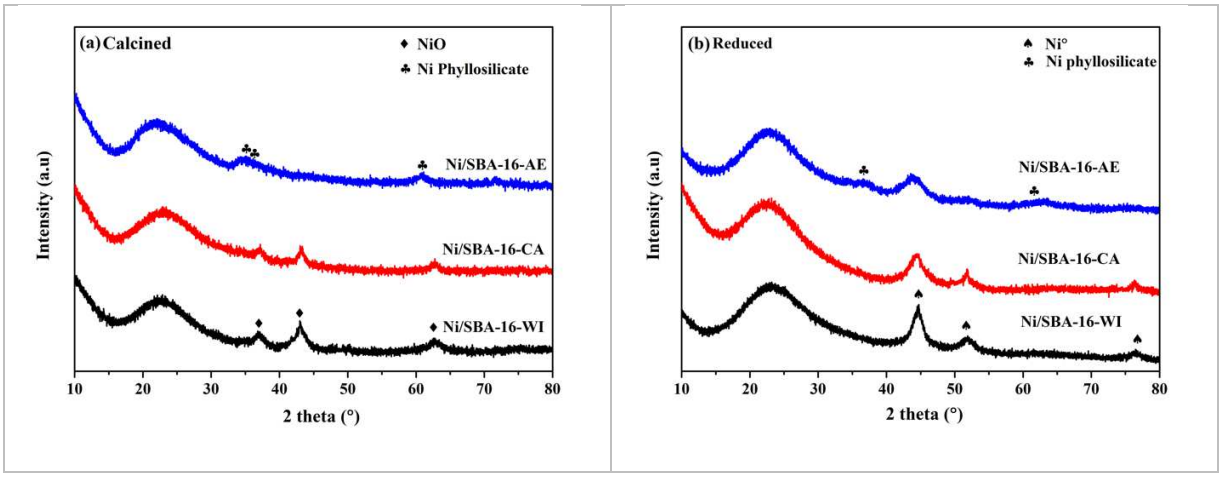

Figure. 2. XRD patterns of the samples after calcination (a) and reduction (b).

The crystallite size of both NiO and Ni^0 is presented in **Table 1**. It shows that crystallite sizes of Ni^0 are almost similar for all catalysts, indicating that for each type of synthesis method the Ni species are highly dispersed on SBA-16. One can also note that compared to the crystallite size of NiO on calcined samples, the crystallite size of Ni^0 decreases for Ni/SBA-16-WI and Ni/SBA-16-CA. This can be attributed to a redistribution of Ni particles occurring during the reduction

process. Indeed, during the reduction it appears that the metallic nickel crystallites (Ni^0 fcc) after reduction are reduced in size by approximately 0.44-0.65 compared to the initial phase (NiO fcc). The crystallite size is expected to decrease due to loss of oxygen according to the literature [42,43]. Nickel (fcc) has a unit cell with edge length a = 2.479 Å and number of formula units Z = 4 [44]. Thus the volume of this cubic cell will be $V_{unitcell}$ = 10,772 Å^3 and the volume per nickel atom is V/(number of Ni atoms in the unit cell) = 2.69 Å^3/Ni atom. Equally the NiO fcc structure has edge length of a = 2.983Å and number of formula units Z=4, while it contains one atom of nickel in the formula [42]. The volume of the cubic cell will be V = 37.485Å^3 and the volume normalized per nickel atom in NiO gives 18.74 Å^3/Ni atom. By introducing the assumption of spherical nickel crystallites, the equation $V_{sphere} = \pi d^3/6$, corresponding to the volume of a sphere, can be applied for both crystals. Solving the equation with respect to crystallite diameters gives $d(Ni_{fcc}) = 0.52\, d(NiO)$ which is in good agreement with the values presented in Table 1.

In order to deeply study the morphology and the particle size of Ni nanoparticles, TEM was performed on the reduced samples. As reported in **Fig. 3**, the presence of ordered cubic cage-like mesoporous structure was identified for all catalysts and was confirmed by the XRD results. For Ni/SBA-16-AE, a partial destruction of mesopores and filamentous morphology can be detected. The latter result clearly indicates the presence of phyllosilicate phases and a partial dissolution of SBA-16 which occurred during ammonia evaporation [31]. From **Fig. 3**, one can see that the smallest average Ni particle size of ca. 5-6 nm is obtained for Ni/SBA-16-AE. From the mean particle sizes presented in **Table 1**, one can also observe that the largest mean particle size of Ni is obtained on the Ni/SBA-16-WI sample. HRTEM was performed and confirmed the presence of particles circular in shape with d-spacing of 2.00 Å which can be assigned to the (111) plane

of metallic nickel (**Fig. 3**). For all studied catalysts the Ni° dispersion (D_{Ni}) was calculated according to method proposed by Bergeret et al.[45]. The results are listed in **Table 1**, showing 10.0%, 12.1% and 16.4% of Ni dispersion, respectively for Ni/SBA-16-WI, Ni/SBA-16-CA and Ni/SBA-16-AE. Higher D_{Ni} was obtained on Ni/SBA-16-CA and Ni/SBA-16-AE, indicating that the CA and AE synthesis methods can improve the Ni dispersion on the SBA-16 matrix. This is in good agreement with the results presented in the study of Hongmanorom et al. [31]. Finally, Ni/SBA-16-AE showed the highest Ni dispersion which is confirmed by the XRD results described above.

3.2 Reducibility of Ni/SBA-16 catalysts

The reducibility of the catalysts was investigated by H_2-TPR. The Ni/SBA-16-WI catalyst showed four reduction peaks (α, β, γ, and θ) located at 348, 452, 627, and 712°C, respectively. These peaks correspond to the reduction of NiO species with different Ni-support interaction (**Fig.4, Table 2**).

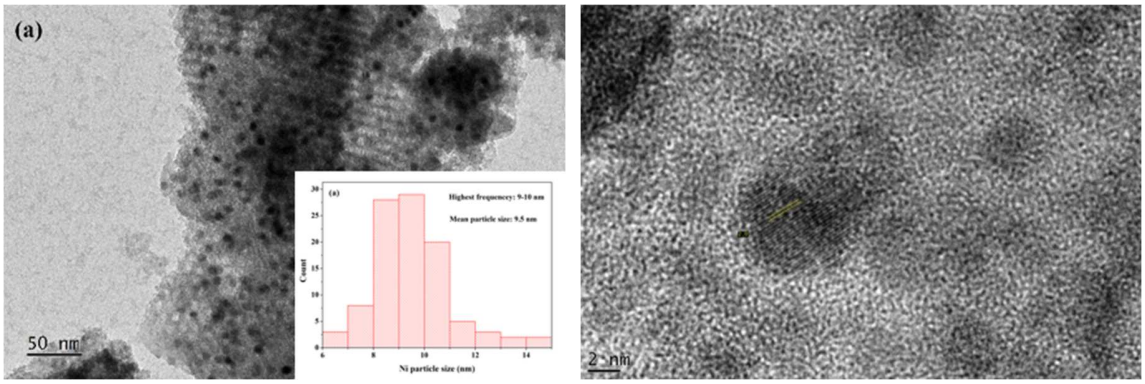

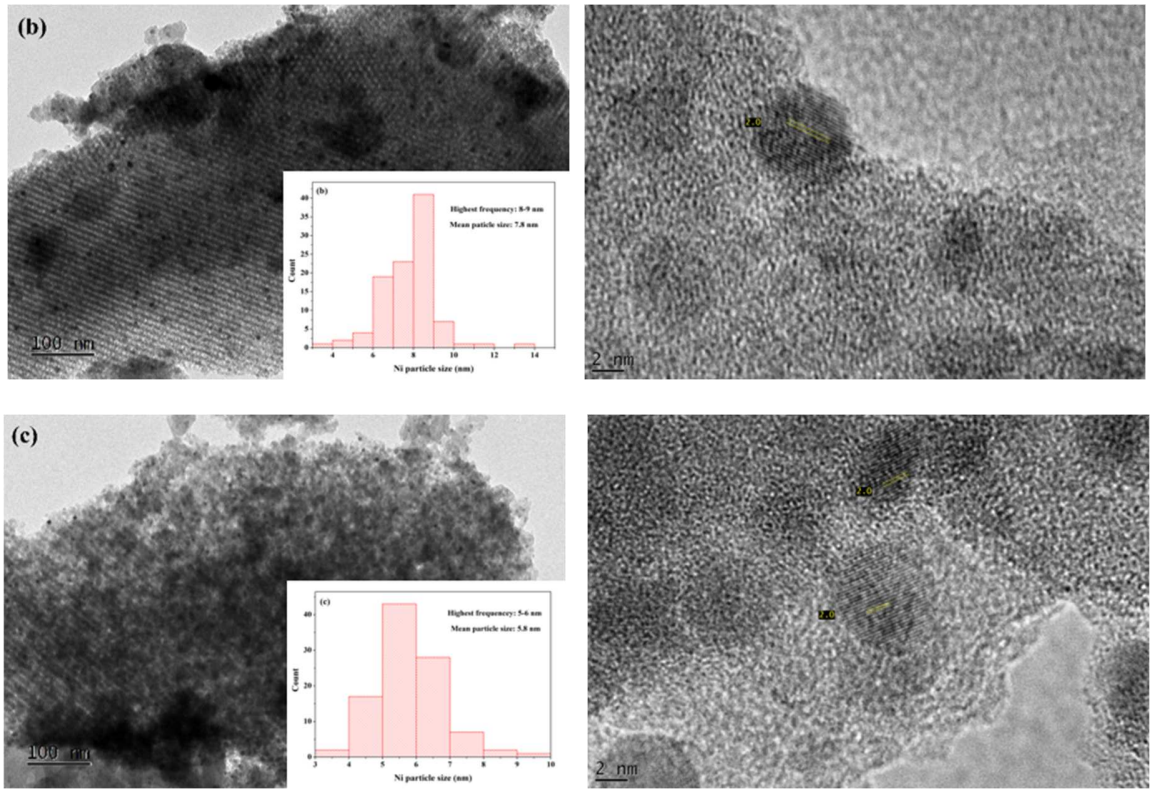

Figure. 3. TEM and HRTEM micrographs and nickel particle size distribution of the reduced catalysts: a) Ni/SBA-16-WI, b) Ni/SBA-16-CA, c) Ni/SBA-16-AE.

The small α peak corresponds to the surface or bulk NiO species in weak interaction with the support. The β peak can be assigned to the NiO intermediately interacting with the support possibly due to the formation of dispersed Ni hydrosilicate as reported elsewhere [9,46]. Furthermore, the peaks γ and θ are attributed to the NiO strongly interacting with the support or tiny NiO nanoparticles within the mesoporous channels [31,47,48]. For Ni/SBA-16-CA, the H_2 consumption γ peak (**Table 2**) corresponds to the reduction of NiO in strong interaction with the support and may be caused by the addition of citric acid during the synthesis. It is worth to note that for Ni/SBA-16-AE, all the reduction peaks shifted to higher temperatures.

Table 2 Reduction peak positions and H_2 consumption calculations from H_2-TPR

Catalyst	Temperature (°C)					H_2 consumption (mmol/g_{cat})					Total (mmol/g_{cat})
	α	β	γ	θ	δ	α	β	γ	θ	δ	
Ni/SBA-16-WI	348	452	627	712	-	0.07	0.80	0.67	0.21	-	1.75
Ni/SBA-16-CA	305	486	598	721	-	0.10	0.42	1.07	0.16	-	1.75
Ni/SBA-16-AE	506	705	799	850	881	0.06	0.71	0.56	0.30	0.14	1.76

The same reduction behavior has been already reported in literature for Ni/SBA-15 catalysts prepared by the AE method. This was clearly attributed to the formation of Ni phyllosilicate [31]. The small α peak of Ni/SBA-16-AE is commonly attributed to the NiO species interacting with the support without the formation of phyllosilicate [31]. The other reduction peaks can be attributed to the reduction of Ni phyllosilicate, which was made up of octahedral sheets with the central Ni^{2+} cation coordinated with six anions (O or OH) and connected to adjacent octahedrons by sharing edges as confirmed elsewhere [31]. The formation of strong Ni-O-Si bonds makes the reduction of NiO more difficult. Thus, from the presented results, the Ni-support interaction strength of the catalysts presents the following ranking: AE>CA>WI.

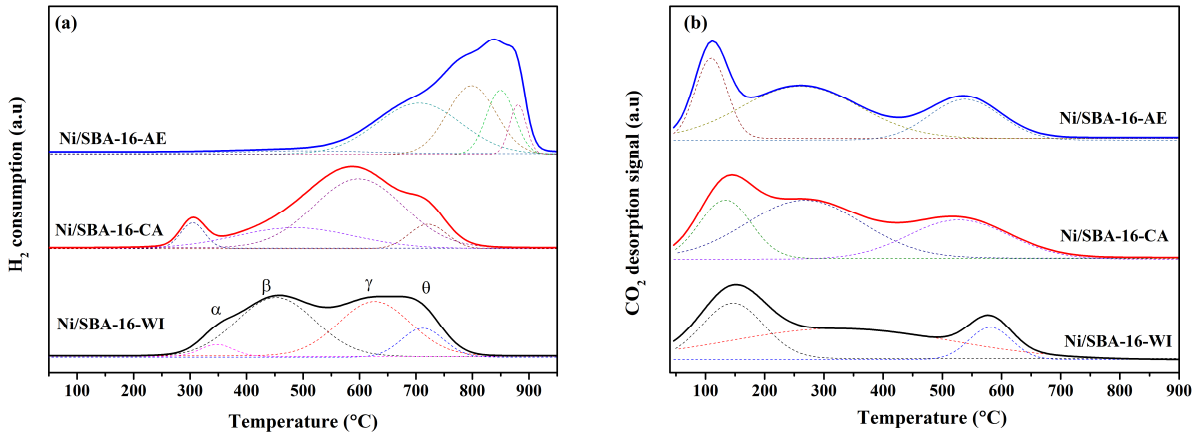

Figure. 4. (a) H_2-TPR profiles of calcined samples. (b) CO_2 desorption profiles for reduced catalysts.

3.3 Basicity of Ni/SBA-16 catalysts

The basicity of catalysts was studied by CO_2-TPD experiment. For all catalysts, the desorption curves can be fitted to three peaks (**Fig. 4b**). The desorption peak at a temperature lower than 200°C can be attributed to the weak basic sites, related to bicarbonate species formed by the interaction between CO_2 and surface OH groups on the SBA-16 [49,50]. The peak at 200-400°C is generally assigned to moderate basic sites, while the peak centered at a temperature higher than 500°C corresponds to the strong basic sites [31,48].

Table 3 Basic sites distribution of catalysts from CO_2-TPD

Catalyst	Basic sites distribution (µmol/g_{cat})			Total basicity (µmol/g_{cat})
	weak	moderate	strong	
Ni/SBA-16-WI	17.8	26.7	8.3	52.8
Ni/SBA-16-CA	12.8	27.1	15.0	54.8
Ni/SBA-16-AE	12.7	31.4	11.1	55.2

The distribution of basic sites (**Table 3)** showed that the Ni/SBA-16 catalysts prepared by different methods have similar total basicity with slightly higher amount medium basic sites for Ni/SBA-16-CA and Ni/SBA-16-AE.

3.4 Catalytic activity and stability in CO_2 reforming of methane

3.4.1. Catalytic activity and stability at 700°C

The synthetized Ni/SBA-16 catalysts were studied in the CRM reaction at 700°C for 10h, followed by 1h run at 750°C. The results corresponding to catalytic performance of catalysts at 700°C are summarized in **Table 4** and **Fig.5**. One can note that rankings in CO_2 and CH_4 conversions at 700°C and the H_2/CO ratio are as follows: AE>WI>CA. By calculating the reaction rate of CO_2 and CH_4 (r_{CO2}, r_{CH4}), it is found that the r_{CO2} or r_{CH4} follows the order:

AE>CA>WI, which means that the Ni/SBA-16 catalysts from CA and AE synthesis methods have higher space time conversion rates compared to the WI catalyst.

Table 4 Catalytic performance of catalysts at 700°C after 1h run

700°C for 1h	CO_2 conversion (%)	CH_4 conversion (%)	H_2/CO ratio	Reaction rate at 700°C (mmol/g_{cat}·s)	
				r_{CO2}	r_{CH4}
Ni/SBA-16-WI	73.1	62.8	0.82	0.19	0.16
Ni/SBA-16-CA	57.1	48.0	0.76	0.23	0.19
Ni/SBA-16-AE	87.3	82.3	0.88	0.32	0.29

From TEM measurements, one can note that the Ni nanoparticle size on AE and CA samples are smaller than for WI. The Ni dispersion followed an order: AE>CA>WI. Meanwhile, the H_2-TPR demonstrated that the Ni-support interaction of the catalysts also followed the order: AE>CA>WI. Thus, we can assume that the Ni dispersion and Ni-support interaction have significant effects on the performance of Ni/SBA-16 catalysts in the CRM reaction. The improved Ni dispersion and Ni-support interaction by CA and AE methods leads to increased reaction rates of CO_2 and CH_4.

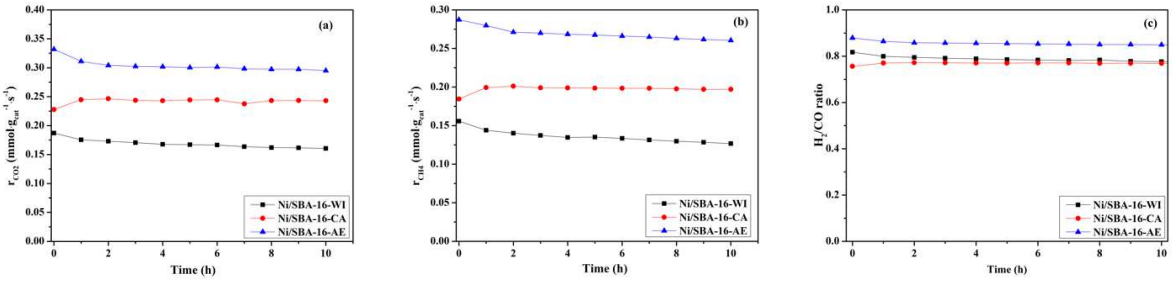

Figure. 5. Stability results for Ni/SBA-16 catalysts at 700 °C for 10 h; (a) rate of CO_2 consumption, (b) rate of CH_4 consumption, and (c) H_2/CO molar ratio versus time-on-stream (TOS) in CRM (CO_2/CH_4/Ar=30/30/40, GHSV=24,000 h^{-1}).

From **Fig.5**, one can note that the Ni/SBA-16-AE catalyst shows higher reaction rate regarding CO_2 and CH_4 with the higher H_2/CO molar ratio during the TOS test. After 10 h of TOS, a distinct loss in reaction rate for Ni/SBA-16-WI is observed already after 1 h regarding the CO_2

reaction rate (from 0.19 to 0.18) and CH_4 conversion (from 0.16 to 0.14). After this first hour of run, the activity of the catalyst tends to slightly decrease. Compared to Ni/SBA-16-WI, the addition of citric acid leads to an improvement of the stability of the Ni/SBA-16-CA catalyst in the TOS evaluation. A slight increase of CO_2 and CH_4 reaction rates, as well as H_2/CO ratio after 10 h of test can be seen from **Fig.6**, which was attributed to promoted Ni-support interaction and Ni distribution. On Ni/SBA-16-AE, similar decreasing trends of reaction rates and H_2/CO ratio were found after the first hour test. However, after this first hour decrease, the reaction rates reached a steady-state. This behavior in reaction rates as a function of TOS can be caused by a redistribution of Ni metal particles at high temperatures, as observed by XRD, and as already reported in the literature [51,52]. Thus, after 10h runs at 750°C, the Ni° particle size calculated from XRD are 5, 5 and 3 nm for Ni/SBA-16-WI, Ni/SBA-16-CA and Ni/SBA-16-AE respectively. These values are similar to the ones obtained prior to the CRM in which d_{Ni° values were 5, 4 and 3 nm, respectively. No sintering was observed which confirms a certain initial stability of the studied catalysts.

To compare the studied catalysts to other supported Ni-based catalysts in CRM at 700°C, Table S1 was presented. One can clearly see that the Ni/SBA-16-AE catalyst led to higher activity than many other catalysts containing noble metals or more expensive supports. The high conversions and reaction rates of Ni/SBA-16-AE catalyst are then attributed in our study to the highly dispersed Ni particles and the strong Ni-support interaction.

3.4.2. Subsequent catalytic activity at 750°C and post run analyses of the catalysts

After the 10h run at 700°C, the temperature was increased up to 750°C, and the catalytic performance of the catalysts was measured (**Table 5**). Also, subsequent characterizations by XRD, TEM and TGA were performed. As expected, it can be observed that the reaction rates

and H_2/CO ratio of the catalysts increase when increasing the temperature from 700 to 750°C (**Table 5**).

Table 5 Catalytic performance of catalysts at 750°C after 1h run

750°C for 1h run	CO_2 conversion (%)	CH_4 conversion (%)	H_2/CO ratio	Reaction rate at **750°C** (mmol/g_{cat}·s)	
				r_{CO2}	r_{CH4}
Ni/SBA-16-WI	90.8	85.3	0.89	0.24	0.22
Ni/SBA-16-CA	66.7	57.6	0.80	0.27	0.23
Ni/SBA-16-AE	92.7	88.6	0.89	0.34	0.31

Thus, at 750°C, for the best catalyst (Ni/SBA-16-AE) the CO_2 and CH_4 reaction rate are 0.34 and 0.31 $mmol \cdot g_{cat}^{-1} \cdot s^{-1}$ and slightly higher than the values obtained after 10h at 700°C.

TGA measurements and TEM images of the used catalysts after test at 750°C are presented in **Fig.6**. From TGA, it is observed that for all the catalysts a distinct weight loss before 100°C is observed. This can be attributed to the evaporation of adsorbed water. From 100 to 400°C, on Ni/SBA-16-CA and Ni/SBA-16-WI a gradual weight loss was observed. This could be attributed to adsorbed species. Finally at T>400°C, the weight loss might be caused by the production of CO_2 from deposited carbon species, as reported elsewhere [51]. A similar trend in the TGA data on the Ni/SBA-16-AE sample is observed for temperatures up to 250°C. However, an increase of the mass was observed in the TGA of the Ni/SBA-16-AE sample above 300°C, which according to literature arises from the oxidation of metallic nickel to nickel oxides [53–56].

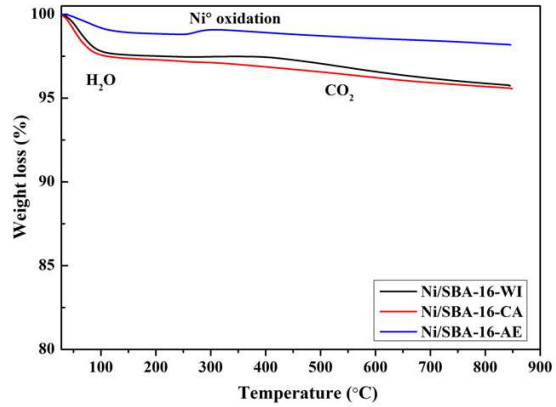
Ni° oxidation
H2O
CO2
Weight loss (%)
Temperature (°C)
Ni/SBA-16-WI
Ni/SBA-16-CA
Ni/SBA-16-AE

(A)

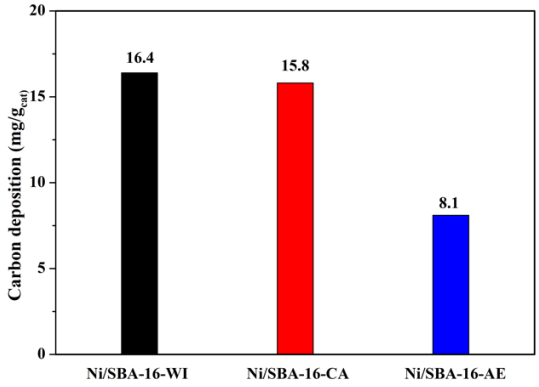
16.4
15.8
8.1
Carbon deposition (mg/gcat)
Ni/SBA-16-WI
Ni/SBA-16-CA
Ni/SBA-16-AE

(B)

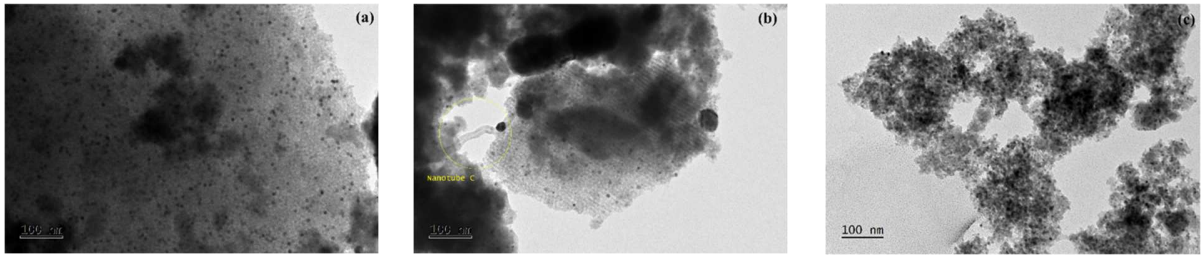
(a)
(b)
(c)
100 nm

(C)

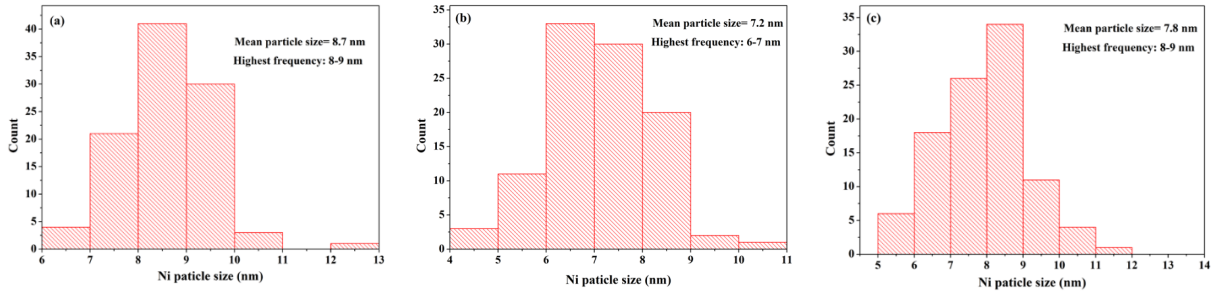
(a)
Mean particle size= 8.7 nm
Highest frequency: 8-9 nm
(b)
Mean particle size= 7.2 nm
Highest frequency: 6-7 nm
(c)
Mean particle size= 7.8 nm
Highest frequency: 8-9 nm
Count
Ni paticle size (nm)

(D)

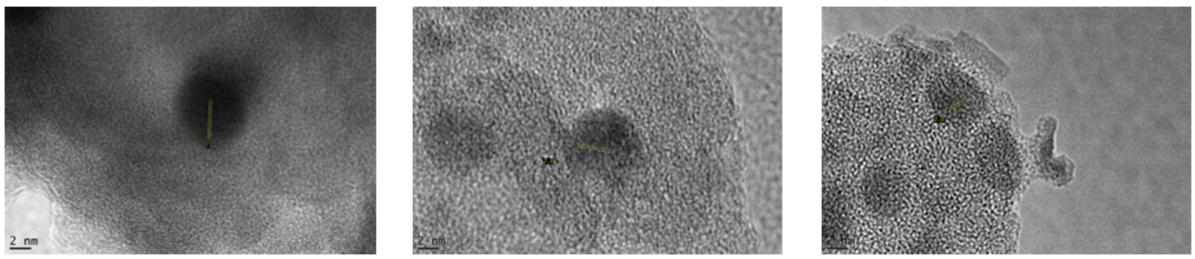

(a) (b) (c)

(E)

Figure. 6. (A) TGA plots of the catalysts after activity tests at 750°C, **(B)** Carbon deposition calculated from TGA on different catalysts, **(C)** TEM micrographs, **(D)** Ni particle size distribution after CRM test at 750°C and (E) HRTEM micrographs (a) Ni/SBA-16-WI, (b) Ni/SBA-16-CA, and (c) Ni/SBA-16-AE.

As shown in Fig.6, the calculated amount of deposited carbon varies from 8.1 to 15.8 and 16.4 $mg \cdot g_{cat}^{-1}$ for Ni/SBA-16-AE, Ni/SBA-16-CA and Ni/SBA-16-WI, respectively. Furthermore, it can be seen that the highest carbon deposition was found on Ni/SBA-16-WI and the lowest amount of carbon was formed on Ni/SBA-16-AE. This could explain the significant activity decrease of Ni/SBA-16-WI catalyst. This latter result can also explain the high stability of Ni/SBA-16-AE after TOS at high temperatures. TEM and HRTEM measurements were also carried out on the catalysts after activity tests at 750°C in order to observe any sintering and carbon deposition. As reported in **Fig. 6**, the ordered mesoporous structure of SBA-16 has remained after CRM tests for all the samples, indicating a good thermal stability of the catalysts structure. No carbon filaments or nanotubes were observed on Ni/SBA-16-AE, whereas a small amount of filaments is observed on Ni/SBA-16-CA and Ni/SBA-16-WI. This is in good agreement with the higher stability and lower carbon deposition on the Ni/SBA-16-AE catalyst. Finally, the Ni particle size distribution and mean Ni particle size was calculated (**Fig 6.**). When compared to the Ni particle sizes on the reduced catalysts reported in **Table 1**, one can note that the Ni particle size distribution does not change significantly after activity tests, indicating no

metal sintering during CRM. This latter result can be explained by the good confinement of the particles in the SBA-16 structure, but also the reoxidation/reduction of Ni particles and the Ni° redistribution occurring during CRM reaction and particularly on the Ni/SBA-16-AE catalyst, confirmed by TGA of the used sample [51].

4. Conclusion

Ni/SBA-16 catalysts prepared by three methods were studied in the CRM reaction. The catalysts synthesized through citric acid-assisted wet impregnation (CA) and ammonia evaporation (AE) showed higher reaction rates (CO_2 and CH_4) than the impregnated Ni/SBA-16 (WI) sample. The high activities are attributed to the highly dispersed Ni^0 particles and to the stronger Ni-support interaction on these catalysts. Ni/SBA-16-AE showed high stability in the CRM reaction due to the absence of nickel sintering and with limited carbon deposition.

Acknowledgment

Chao Sun thanks the China Scholarship Council (CSC) for the scholarship in his Ph.D. studying at Sorbonne Université. Katarzyna Świrk is MSCA-IF researcher at the Norwegian University of Science and Technology in Norway. This project has received funding from the European Union's Horizon 2020 research and innovation programme under the Marie Skłodowska-Curie grant agreement No 892571. Thanks are due to Dr. Marco Fabbiani for SAXS measurements, and to Fédération de Recherche FR2482 becoming « Fédération de Chimie et Matériaux de Paris-Centre » avec l'acronyme FCMat for TEM facilities.

References

[1] P. Nema, S. Nema, P. Roy, An overview of global climate changing in current scenario and mitigation action, Renew. Sustain. Energy Rev. 16 (2012) 2329–2336.

https://doi.org/10.1016/j.rser.2012.01.044.

[2] S.C. Peter, Reduction of CO2 to chemicals and fuels: A solution to global warming and energy crisis, ACS Energy Lett. 3 (2018) 1557–1561. https://doi.org/10.1021/acsenergylett.8b00878.

[3] L. Fu, K.K.R. Datta, K. Spyrou, G. Qi, A. Sardar, M.M. Khader, R. Zboril, E.P. Giannelis, Phyllosilicate nanoclay-based aqueous nanoparticle sorbent for CO2 capture at ambient conditions, Appl. Mater. Today. 9 (2017) 451–455. https://doi.org/10.1016/j.apmt.2017.09.009.

[4] M.E. Boot-Handford, J.C. Abanades, E.J. Anthony, M.J. Blunt, S. Brandani, N. Mac Dowell, J.R. Fernández, M.C. Ferrari, R. Gross, J.P. Hallett, R.S. Haszeldine, P. Heptonstall, A. Lyngfelt, Z. Makuch, E. Mangano, R.T.J. Porter, M. Pourkashanian, G.T. Rochelle, N. Shah, J.G. Yao, P.S. Fennell, Carbon capture and storage update, Energy Environ. Sci. 7 (2014) 130–189. https://doi.org/10.1039/c3ee42350f.

[5] J. Artz, T.E. Müller, K. Thenert, J. Kleinekorte, R. Meys, A. Sternberg, A. Bardow, W. Leitner, Sustainable Conversion of Carbon Dioxide: An Integrated Review of Catalysis and Life Cycle Assessment, Chem. Rev. 118 (2018) 434–504. https://doi.org/10.1021/acs.chemrev.7b00435.

[6] S. Kar, R. Sen, A. Goeppert, G.K.S. Prakash, Integrative CO2 Capture and hydrogenation to methanol with reusable catalyst and amine: Toward a carbon neutral methanol economy, J. Am. Chem. Soc. 140 (2018) 1580–1583. https://doi.org/10.1021/jacs.7b12183.

[7] C. Sun, P. Beaunier, V. La Parola, L. F. Liotta, P. Da Costa, Ni/CeO2 Nanoparticles Promoted by Yttrium Doping as Catalysts for CO2 Methanation, ACS Appl. Nano Mater.

3 (2020) 12355–12368. https://doi.org/10.1021/acsanm.0c02841.

[8] Y. Wang, L. Yao, Y. Wang, S. Wang, Q. Zhao, D. Mao, C. Hu, Low-Temperature Catalytic CO2 Dry Reforming of Methane on Ni-Si/ZrO2 Catalyst, ACS Catal. 8 (2018) 6495–6506. https://doi.org/10.1021/acscatal.8b00584.

[9] S. Zhang, S. Muratsugu, N. Ishiguro, M. Tada, Ceria-doped Ni/SBA-16 catalysts for dry reforming of methane, ACS Catal. 3 (2013) 1855–1864. https://doi.org/10.1021/cs400159w.

[10] Y. Zhang, G. Jacobs, D.E. Sparks, M.E. Dry, B.H. Davis, CO and CO2 hydrogenation study on supported cobalt Fischer-Tropsch synthesis catalysts, Catal. Today. 71 (2002) 411–418. https://doi.org/10.1016/S0920-5861(01)00468-0.

[11] A. Martínez, C. López, F. Márquez, I. Díaz, Fischer-Tropsch synthesis of hydrocarbons over mesoporous Co/SBA-15 catalysts: The influence of metal loading, cobalt precursor, and promoters, J. Catal. 220 (2003) 486–499. https://doi.org/10.1016/S0021-9517(03)00289-6.

[12] M. Akri, S. Zhao, X. Li, K. Zang, A.F. Lee, M.A. Isaacs, W. Xi, Y. Gangarajula, J. Luo, Y. Ren, Y.T. Cui, L. Li, Y. Su, X. Pan, W. Wen, Y. Pan, K. Wilson, L. Li, B. Qiao, H. Ishii, Y.F. Liao, A. Wang, X. Wang, T. Zhang, Atomically dispersed nickel as coke-resistant active sites for methane dry reforming, Nat. Commun. 10 (2019) 1–10. https://doi.org/10.1038/s41467-019-12843-w.

[13] K. Han, Y. Wang, S. Wang, Q. Liu, Z. Deng, F. Wang, Narrowing band gap energy of CeO2 in (Ni/CeO2)@SiO2 catalyst for photothermal methane dry reforming, Chem. Eng. J. 421 (2021) 129989. https://doi.org/10.1016/j.cej.2021.129989.

[14] K. Han, S. Wang, Q. Liu, F. Wang, Optimizing the Ni/Cu Ratio in Ni-Cu Nanoparticle

Catalysts for Methane Dry Reforming, ACS Appl. Nano Mater. 4 (2021) 5340–5348. https://doi.org/10.1021/acsanm.1c00673.

[15] F. Wang, K. Han, W. Yu, L. Zhao, Y. Wang, X. Wang, H. Yu, W. Shi, Low Temperature CO2 Reforming with Methane Reaction over CeO2-Modified Ni@SiO2Catalysts, ACS Appl. Mater. Interfaces. 12 (2020) 35022–35034. https://doi.org/10.1021/acsami.0c09371.

[16] B. Han, L. Zhao, F. Wang, L. Xu, H. Yu, Y. Cui, J. Zhang, W. Shi, Effect of Calcination Temperature on the Performance of the Ni@SiO2Catalyst in Methane Dry Reforming, Ind. Eng. Chem. Res. 59 (2020) 13370–13379. https://doi.org/10.1021/acs.iecr.0c01213.

[17] K. Han, W. Yu, L. Xu, Z. Deng, H. Yu, F. Wang, Reducing carbon deposition and enhancing reaction stability by ceria for methane dry reforming over Ni@SiO2@CeO2 catalyst, Fuel. 291 (2021) 120182. https://doi.org/10.1016/j.fuel.2021.120182.

[18] F. Wang, K. Han, L. Xu, H. Yu, W. Shi, Ni/SiO2 catalyst prepared by strong electrostatic adsorption for a low-temperature methane dry reforming reaction, Ind. Eng. Chem. Res. 60 (2021) 3324–3333. https://doi.org/10.1021/acs.iecr.0c06020.

[19] K. Han, S. Xu, Y. Wang, S. Wang, L. Zhao, J. Kambonde, H. Yu, W. Shi, F. Wang, Confining Ni and ceria in silica shell as synergistic multifunctional catalyst for methane dry reforming reaction, J. Power Sources. 506 (2021) 230232. https://doi.org/10.1016/j.jpowsour.2021.230232.

[20] J.H. Kim, D.J. Suh, T.J. Park, K.L. Kim, Effect of metal particle size on coking during CO2 reforming of CH4 over Ni-alumina aerogel catalysts, Appl. Catal. A Gen. 197 (2000) 191–200. https://doi.org/10.1016/S0926-860X(99)00487-1.

[21] H.S. Bengaard, J.K. Nørskov, J. Sehested, B.S. Clausen, L.P. Nielsen, A.M. Molenbroek, J.R. Rostrup-Nielsen, Steam reforming and graphite formation on Ni catalysts, J. Catal.

209 (2002) 365–384. https://doi.org/10.1006/jcat.2002.3579.

[22] N. Wang, X. Yu, K. Shen, W. Chu, W. Qian, Synthesis, characterization and catalytic performance of Ce-SBA-15 supported nickel catalysts for methane dry reforming to hdrogen and syngas, Int. J. Hydrogen Energy. 37 (2012) 19–30. https://doi.org/10.1016/j.ijhydene.2011.03.138.

[23] A. Albarazi, M.E. Gálvez, P. Da Costa, Synthesis strategies of ceria-zirconia doped Ni/SBA-15 catalysts for methane dry reforming, Catal. Commun. 59 (2015) 108–112. https://doi.org/10.1016/j.catcom.2014.09.050.

[24] Z. Taherian, V. Shahed Gharahshiran, A. Khataee, F. Meshkani, Y. Orooji, Comparative study of modified Ni catalysts over mesoporous CaO-Al2O3 support for CO2/methane reforming, Catal. Commun. 145 (2020) 106100. https://doi.org/10.1016/j.catcom.2020.106100.

[25] P. Hongmanorom, J. Ashok, P. Chirawatkul, S. Kawi, Interfacial synergistic catalysis over Ni nanoparticles encapsulated in mesoporous ceria for CO2 methanation, Appl. Catal. B Environ. 297 (2021) 120454. https://doi.org/10.1016/j.apcatb.2021.120454.

[26] K. Mette, S. Kühl, A. Tarasov, M.G. Willinger, J. Kröhnert, S. Wrabetz, A. Trunschke, M. Scherzer, F. Girgsdies, H. Düdder, K. Kähler, K.F. Ortega, M. Muhler, R. Schlögl, M. Behrens, T. Lunkenbein, High-Temperature Stable Ni Nanoparticles for the Dry Reforming of Methane, ACS Catal. 6 (2016) 7238–7248. https://doi.org/10.1021/acscatal.6b01683.

[27] C.C. Chong, L.P. Teh, H.D. Setiabudi, Syngas production via CO 2 reforming of CH 4 over Ni-based SBA-15: Promotional effect of promoters (Ce, Mg, and Zr), Mater. Today Energy. 12 (2019) 408–417. https://doi.org/10.1016/j.mtener.2019.04.001.

[28] M. HUO, L. LI, X. ZHAO, Y. ZHANG, J. LI, Synthesis of Ni-based catalysts supported on nitrogen-incorporated SBA-16 and their catalytic performance in the reforming of methane with carbon dioxide, J. Fuel Chem. Technol. 45 (2017) 172–181. https://doi.org/10.1016/S1872-5813(17)30012-9.

[29] Zahra Taherian, A. Khataee, Y. Orooji, Nickel-based nanocatalysts promoted over MgO-modified SBA-16 for dry reforming of methane for syngas production: Impact of support and promoters, J. Energy Inst. (2021). https://doi.org/10.1016/j.joei.2021.04.005.

[30] W. Li, Y. Liu, M. Mu, F. Ding, Z. Liu, X. Guo, C. Song, Organic acid-assisted preparation of highly dispersed Co/ZrO2 catalysts with superior activity for CO2 methanation, Appl. Catal. B Environ. 254 (2019) 531–540. https://doi.org/10.1016/j.apcatb.2019.05.028.

[31] P. Hongmanorom, J. Ashok, G. Zhang, Z. Bian, M.H. Wai, Y. Zeng, S. Xi, A. Borgna, S. Kawi, Enhanced performance and selectivity of CO2 methanation over phyllosilicate structure derived Ni-Mg/SBA-15 catalysts, Appl. Catal. B Environ. 282 (2021) 119564. https://doi.org/10.1016/j.apcatb.2020.119564.

[32] C. Sun, P. Beaunier, P. Da Costa, Effect of ceria promotion on the catalytic performance of Ni/SBA-16 catalysts for CO2 methanation, Catal. Sci. Technol. 10 (2020) 6330–6341. https://doi.org/10.1039/d0cy00922a.

[33] C. Sun, K. Świrk, Y. Wang, K.S. Scheidl, D.W. Breiby, M. Rønning, C. Hu, P. Da Costa, Tailoring the yttrium content in Ni-Ce-Y/SBA-15 mesoporous silicas for CO2 methanation, Catal. Today. (2021). https://doi.org/10.1016/j.cattod.2021.07.031.

[34] C. Sun, K. Świrk, D. Wierzbicki, M. Motak, T. Grzybek, P. Da Costa, On the effect of yttrium promotion on Ni-layered double hydroxides-derived catalysts for hydrogenation of CO2 to methane, Int. J. Hydrogen Energy. (2020).

https://doi.org/10.1016/j.ijhydene.2020.03.202.

[35] O.C. Gobin, Y. Wan, D. Zhao, F. Kleitz, S. Kaliaguine, Mesostructured silica SBA-16 with tailored intrawall porosity part 1: Synthesis and characterization, J. Phys. Chem. C. 111 (2007) 3053–3058. https://doi.org/10.1021/jp0635765.

[36] B.L. Newalkar, J. Olanrewaju, S. Komarneni, Microwave-hydrothermal synthesis and characterization of zirconium substituted SBA-15 mesoporous silica, J. Phys. Chem. B. 105 (2001) 8356–8360. https://doi.org/10.1021/jp010889l.

[37] C. Ciotonea, B. Dragoi, A. Ungureanu, A. Chirieac, S. Petit, S. Royer, E. Dumitriua, Nanosized transition metals in controlled environments of phyllosilicate–mesoporous silica composites as highly thermostable and active catalysts, Chem. Commun. 49 (2013) 7665–7667. https://doi.org/10.1039/c3cc43197e.

[38] A. Rodriguez-Gomez, R. Pereñiguez, A. Caballero, Nickel Particles Selectively Confined in the Mesoporous Channels of SBA-15 Yielding a Very Stable Catalyst for DRM Reaction, J. Phys. Chem. B. 122 (2018) 500–510. https://doi.org/10.1021/acs.jpcb.7b03835.

[39] M. González-Castaño, J.C.N. de Miguel, A. Penkova, M.A. Centeno, J.A. Odriozola, H. Arellano-Garcia, Ni/YMnO3 perovskite catalyst for CO2 methanation, Appl. Mater. Today. 23 (2021) 27–30. https://doi.org/10.1016/j.apmt.2021.101055.

[40] C. Sun, J. Krstic, V. Radonjic, M. Stankovic, P. Da Costa, The effect of Ni precursor salts on diatomite supported Ni-Mg catalysts in methanation of CO2, Mater. Sci. Forum. 1016 (2021) 1417–1422. https://doi.org/https://doi.org/10.4028/www.scientific.net/MSF.1016.1417.

[41] Z. Li, Y. Kathiraser, J. Ashok, U. Oemar, S. Kawi, Simultaneous tuning porosity and

basicity of nickel@nickel-magnesium phyllosilicate core-shell catalysts for CO2 reforming of CH4, Langmuir. 30 (2014) 14694–14705. https://doi.org/10.1021/la503340s.

[42] M. Rønning, N.E. Tsakoumis, A. Voronov, R.E. Johnsen, P. Norby, W. Van Beek, Ø. Borg, E. Rytter, A. Holmen, Combined XRD and XANES studies of a Re-promoted Co/γ-Al 2O3 catalyst at Fischer-Tropsch synthesis conditions, Catal. Today. 155 (2010) 289–295. https://doi.org/10.1016/j.cattod.2009.10.010.

[43] L.A. García-Cerda, K.M. Bernal-Ramos, S.M. Montemayor, M.A. Quevedo-López, R. Betancourt-Galindo, D. Bueno-Báques, Preparation of hcp and fcc Ni and Ni/NiO nanoparticles using a citric acid assisted Pechini-type method, J. Nanomater. 2011 (2011). https://doi.org/10.1155/2011/162495.

[44] K. Persson, Materials Data on Li6Fe3Co7O20 (SG: 10) by Materials Project, No. Mp-763066. Lawrence Berkeley Natl. Lab.(LBNL), Berkeley, CA (United States). LBNL Mater. Proj. (2014). https://doi.org/10.17188/1199153.

[45] G. Bergeret, P. Gallezot, Particle Size and Dispersion Measurements, in: Handb. Heterog. Catal., American Cancer Society, 2008: pp. 738–765. https://doi.org/https://doi.org/10.1002/9783527610044.hetcat0038.

[46] H.D. Setiabudi, C.C. Chong, S.M. Abed, L.P. Teh, S.Y. Chin, Comparative study of Ni-Ce loading method: Beneficial effect of ultrasonic-assisted impregnation method in CO2 reforming of CH4 over Ni-Ce/SBA-15, J. Environ. Chem. Eng. 6 (2018) 745–753. https://doi.org/10.1016/j.jece.2018.01.001.

[47] J. Van De Loosdrecht, A.M. Van Der Kraan, A.J. Van Dillen, J.W. Geus, Metal-support interaction: Titania-supported and silica-supported nickel catalysts, J. Catal. 170 (1997) 217–226. https://doi.org/10.1006/jcat.1997.1741.

[48] L. Xu, H. Yang, M. Chen, F. Wang, D. Nie, L. Qi, X. Lian, H. Chen, M. Wu, CO2 methanation over Ca doped ordered mesoporous Ni-Al composite oxide catalysts: The promoting effect of basic modifier, J. CO2 Util. 21 (2017) 200–210. https://doi.org/10.1016/j.jcou.2017.07.014.

[49] J. Ashok, Y. Kathiraser, M.L. Ang, S. Kawi, Bi-functional hydrotalcite-derived NiO-CaO-Al2O3 catalysts for steam reforming of biomass and/or tar model compound at low steam-to-carbon conditions, Appl. Catal. B Environ. 172–173 (2015) 116–128. https://doi.org/10.1016/j.apcatb.2015.02.017.

[50] M. Romero-Sáez, A.B. Dongil, N. Benito, R. Espinoza-González, N. Escalona, F. Gracia, CO2 methanation over nickel-ZrO2 catalyst supported on carbon nanotubes: A comparison between two impregnation strategies, Appl. Catal. B Environ. 237 (2018) 817–825. https://doi.org/10.1016/j.apcatb.2018.06.045.

[51] Y. Wang, Q. Zhao, Y. Wang, C. Hu, P. Da Costa, One-Step Synthesis of Highly Active and Stable Ni-ZrOx for Dry Reforming of Methane, Ind. Eng. Chem. Res. 59 (2020) 11441–11452. https://doi.org/10.1021/acs.iecr.0c01416.

[52] K. Świrk, M.E. Gálvez, M. Motak, T. Grzybek, M. Rønning, P. Da Costa, Yttrium promoted Ni-based double-layered hydroxides for dry methane reforming, J. CO2 Util. (2018). https://doi.org/10.1016/j.jcou.2018.08.004.

[53] K. Świrk, M. Rønning, M. Motak, P. Beaunier, P. Da Costa, T. Grzybek, Ce- and Y-modified double-layered hydroxides as catalysts for dry reforming of methane : On the effect of yttrium promotion, Catalysts. 9 (2019) 56–74. https://doi.org/10.3390/catal9010056.

[54] A.I. Tsyganok, T. Tsunoda, S. Hamakawa, K. Suzuki, K. Takehira, T. Hayakawa, Dry

reforming of methane over catalysts derived from nickel-containing Mg-Al layered double hydroxides, J. Catal. 213 (2003) 191–203. https://doi.org/10.1016/S0021-9517(02)00047-7.

[55] K. Świrk, M. Rønning, M. Motak, T. Grzybek, P. Da Costa, Synthesis strategies of Zr- and Y-promoted mixed oxides derived from double-layered hydroxides for syngas production via dry reforming of methane, Int. J. Hydrogen Energy. (2020). https://doi.org/10.1016/j.ijhydene.2020.04.239.

[56] K. Świrk, J. Grams, M. Motak, P. Da Costa, T. Grzybek, Understanding of tri-reforming of methane over Ni / Mg / Al hydrotalcite-derived catalyst for CO2 utilization from flue gases from natural gas-fired power plants, J. CO2 Util. 42 (2020) 101317–101323. https://doi.org/10.1016/j.jcou.2020.101317.

Ammonia Evaporation

Citric Acid

Ethanol

$Ni(NO_3)_2 \cdot 6H_2O$

AE

CA

WI

Ni-Phyllosilicate

NiOx

NiOx

Calcination

Reductio

d_{Ni^0}

$CO_2 + CH_4$

$2CO + 2H_2$